# Synthesis and Preclinical Fluorescence Imaging of Dually Functionalized Antibody Conjugates Targeting Endothelin Receptor-Positive Tumors

Delphine Vivier, Marie Hautière, Donovan Pineau, Pierre-Alix Dancer, Amaury Herbet, Jean-Philippe Hugnot, Claire Bernhard, Victor Goncalves, Charles Truillet, Didier Boquet, et al.

# Synthesis and preclinical fluorescence imaging of dually-functionalized antibody conjugates targeting endothelin receptors positive tumors

Delphine Vivier[1+], Marie Hautière[2,3+], Donovan Pineau[4], Pierre-Alix Dancer[5], Amaury Herbet[2], Jean-Philippe Hugnot[4], Claire Bernhard[1], Victor Goncalves[1], Charles Truillet[3], Didier Boquet[2*], Franck Denat[1*]

**Authors affiliations**

[1] Université de Bourgogne, ICMUB UMR CNRS 6302, 21000 Dijon, France

[2] Université Paris-Saclay, CEA, DMTS, SPI, 91191 Gif-sur-Yvette, France

[3] Université Paris-Saclay, CEA, CNRS, Inserm, BioMaps, 91401 Orsay, France

[4] Université de Montpellier, IGF, INSERM U 1191 - CNRS UMR 5203, 34094 Montpellier, France

[5] Kaer Labs, 44300 Nantes, France

[+] These authors contributed equally

[*] Corresponding and co last authors: Franck.Denat@u-bourgogne.fr ; Didier.BOQUET@cea.fr

**ABSTRACT**

For the past two decades, the emerging role of the endothelin axis (ET) in cancer has been extensively investigated and its involvement in several mechanisms described as “hallmarks of cancer” has clearly highlighted its potential as a therapeutic target. Despite the growing interest in finding effective anti-cancer drugs, no breakthrough treatment has successfully made its way to the market. Recently, our team reported the development of a new immunoPET probe targeting the endothelin A receptor ($ET_A$, one of the endothelin receptors), that allows the successful detection of $ET_A^+$ glioblastoma, paving the way for the elaboration of novel antibody-based strategies. In this study, we describe the synthesis of two PET/NIRF (near infrared fluorescence) dually-functionalized imaging agents, directed against $ET_A$ or $ET_B$, that could be used to detect $ET^+$ tumors and select patients that will be eligible for fluorescence-guided surgery (FGS). Both imaging modalities were brought together using a highly versatile tetrazine platform bearing IRDye800CW fluorophore and desferrioxamine for $^{89}$Zr chelation. This so-called Monomolecular Multimodal Imaging Probe (MOMIP) was then “clicked”, via an inverse Electron Demand Diels-Alder reaction (iEDDA), to antibodies conjugated site-specifically with a transcyclooctene group. This approach has

led to homogenous and well-defined constructs that retained their high affinity and high specificity for their respective target, as shown by flow cytometry and NIRF in vivo imaging experiments in nude mice bearing CHO-$ET_A$ and CHO-$ET_B$ tumors. Ultimately, these bimodal immunoconjugates could be used to improve outcomes of patients with $ET^+$ tumors.

**KEYWORDS**

Endothelin axis, NIRF imaging, site-specific conjugation, monomolecular multimodal imaging probe (MOMIP), Fluorescence-Guided Surgery.

## INTRODUCTION

Comprising three 21-mer peptides (ET-1, ET-2 and ET-3) and two G-protein-coupled receptors (GPCR) subtypes ($ET_A$ and $ET_B$), the endothelin axis was first identified as a potent endogenous vasoconstrictor and mediator of cardiovascular and renal disorders.[1] Since early 2000's, dysregulations of the ET axis have been linked to the growth and progression of various tumors, inducing cell proliferation, survival, angiogenesis and metastatic spread.[2–5] In total, aberrantly activation of endothelin-1 receptors seems to be involved in twelve of the fourteen hallmarks of cancer described by Hanahan,[6] emphasizing the potential of ET axis as a therapeutic target. Several antagonists – targeting either $ET_A$ (Zibotentan, Atrasentan), $ET_B$ (SPI 1620) or both (Bosentan, Macitentan) – have been developed and pushed toward the clinics.[5,7] However, despite promising preclinical data and many clinical trials encompassing various cancers (such as melanoma, glioma, pancreatic cancer, prostate cancer), none of the candidates has successfully reached the market. The elevated concentration of ET-1 within the tumoral environment coupled with its strong affinity for its receptor presents a significant challenge for an antagonist to compete, that could be responsible for the discrepancy between preclinical and clinical results. To circumvent this issue, two high-affinity antibodies – that do not compete with ET-1 – named Rendomab A63 (RA63) and Rendomab B49 (RB49), directed respectively against $ET_A$ and $ET_B$ receptors have been patented.[8,9] We have recently demonstrated that a chimeric version of RA63 called xiRA63 could be randomly labeled with zirconium-89 ($^{89}Zr$, $t_{1/2}$ = 3.3 days) and used to detect $ET_A^+$ glioblastoma in a mouse model xenografted orthotopically with patient derived Gli7 GSC, thanks to immunoPET imaging.[10] Likewise, a chimeric version of the latter, xiRB49, was modified with a cytotoxic molecule to obtain an antibody-drug conjugate showing a very

high efficacy to treat $ET_B^+$ melanoma with no notable side effects on mice (Herbet et al., in preparation). These promising results prompted us to develop new bimodal imaging immunotracers that could help improving outcomes of patients with $ET^+$ tumors.

In many types of cancer, surgery remains a key treatment option. For example, more than 50% of patients diagnosed with stage I or II breast, colorectum or lung cancer will undergo surgery.[11] The extent of the resection is often linked to the prognosis. Indeed, the presence of residual tumor cells, called positive margins, is a strong predictor of tumor recurrence. Achieving a complete resection with the naked eye can be tricky. To obtain negative margins, surgeon can turn to intraoperative histopathological analysis of frozen tumor margins but the process is time-consuming. Non-optical imaging methods like intraoperative CT and MRI can also be helpful but those methods are costly and their use disrupts the surgical procedure, increasing operative and anesthesia times. In contrast, Fluorescence Guided Surgery (FGS) is a low-cost technique that offers high sensitivity, ease of use and safety to delineate tumor margins.[12,13] Several fluorophores are already approved and used in clinic, like indocyanine green (ICG), fluorescein or 5-ALA.[12] However, those imaging agents do not specifically target cancer cells and the tumor-to-background ratio can be disappointing. In addition to non-specific signal, tumors heterogeneity and the difficulty to predict which patients could benefit from FGS may explain these mixed results. To overcome some of those limitations, the fluorophore can be conjugated to a targeting vector such as a monoclonal antibody.[14] For example, the FDA-approved IRDye800CW has been conjugated to various antibodies and is currently involved in promising clinical trials.[15–18] Along with specificity, stratification of patients could greatly improve FGS outcomes. Bimodal imaging, combining a pre-operative imaging technique and real-time fluorescence imaging is an attractive solution to increase the extent of tumor resection.[19,20] Indeed, nuclear medicine imaging – either single-photon emission computed tomography (SPECT) or positron emission tomography (PET) – can be used to detect tumors and select patients that will be eligible to FGS.[21–23] Several strategies can be employed for the synthesis of such bimodal bioconjugates.[24,25] Random and sequential introduction of the two probes leads to a highly heterogeneous mixture of millions of conjugates, with different numbers of probes per antibody, various ratios of the two probes, and a multitude of possible locations of these probes on the protein. This may have deleterious consequences, including a poorly reproducible synthesis, a potential effect on the photophysical properties of the dye, and,

more importantly, different pharmacokinetics and *in vivo* fate of the different bioconjugates, or even a loss of affinity of the antibodies for their target.[26–29] For these reasons, we focused on a more elegant strategy involving: i) the preparation of a so-called MOnomolecular Multimodal Imaging Probe (MOMIP) bringing together the dye and the chelator on a tetrazine platform, ii) the click conjugation of this MOMIP on the antibodies, previously modified site-specifically with a *trans*-cyclooctene (TCO) group, through an inverse electron-demand Diels-Alder (iEDDA) reaction. In this manuscript, we wish to report the synthesis of two dually-functionalized immunoconjugates – containing both a NIR fluorophore (IRDye800CW) for fluorescence-guided surgery and Desferrioxamine (DFO), the standard chelating agent so far for $^{89}$Zr-labeling of antibodies – and the *in vitro* validation of their ability to bind ET receptors on CHO-$ET_A$ and CHO-$ET_B$ cells. We also conducted a preliminary in vivo fluorescence imaging study to demonstrate the potential of the conjugates to accumulate in $ET_A^+$ and $ET_B^+$ tumors implanted subcutaneously in mouse models.

## EXPERIMENTAL PROCEDURES

### Instruments and methods

Purifications by semi-preparative HPLC were performed on an UltiMate 3000 system Dionex (Thermo Scientific) equipped with an UV-visible detector, on the following columns: BetaBasic-18 column (Thermo Scientific) (5 µm, 150 Å) at 20 mL/minutes, or Hypersil GOLD column 100 x 10 (Thermo Scientific) (5 µm, 175 Å) at 3.5 mL/min, with HPLC grade eluents. Unless specified otherwise, purifications were performed using acetonitrile and water, both supplemented with 0.1% of trifluoroacetic acid. The fractions of interest were analyzed by HPLC-MS, pooled, concentrated under reduced pressure to remove organic solvents, and freeze-dried.

High performance liquid chromatography (HPLC) analyses were performed on an UltiMate 3000 system Dionex (Thermo Scientific) equipped with a DAD detector and coupled to a low-resolution mass spectrometry detector MSQ Plus (Thermo Scientific) with an ESI source. Separation was achieved using an RP Kinetex™ column (Phenomenex) (2.6 µm, 100 Å, 50 Å, 2.1 mm) with HPLC quality solvents: A: $H_2O$ + 0.1% FA and B: MeCN + 0.1% FA. Analyses were performed with the following gradient program: 5% to 100% of B in 5 min, 100% B for 1.5 min, 100% to 5% B in 0.1 min and 5% B for 1.9 min, at a flow rate of 0.5 mL/min. NMR spectra were acquired on a Bruker NMR spectrometer 500 MHz Avance DRX. HRMS spectra

were recorded on a mass spectrometer LTQ Orbitrap XL (Thermo Scientific) using an ESI source.

Bioconjugation reactions were followed by reverse phase HPLC (Vanquish, Thermo Fisher Scientific) coupled to a high-resolution Orbitrap mass spectrometer (Exploris 240, Thermo Fisher Scientific) using an ESI source (positive mode). Before analysis, a small sample was digested with the IDES enzyme (Promega): 20 µg of conjugate were mixed with 20U of IDES (10U/µL) and the volume was adjusted to 10 µL with deionized water. The reaction mixture was incubated at 37°C for 60 min. HPLC: A MabPac RP column (2.1 mm x 100 mm, 4µm, Thermo Fisher Scientific) was used at 80°C (denaturing conditions), with a flow rate of 0.5 mL/min and a gradient 20-45% B in 6 min (eluents A: $H_2O$ + 0.02% TFA + 0.08% FA and B: ACN + 0.02% TFA + 0.08% FA). Mass: Full scan data were acquired at resolving power 30000 at m/z 200 in the m/z range 1000 – 4000. Data were analyzed with FreeStyle and BioPharma Finder 4.1 software (both Thermo Fisher Scientific). High-resolution mass spectra were deconvoluted using the Xtract function for IDES fragments (≈ 25 kDA) and ReSpect function for intact antibody (≈ 150 kDa). Degrees of labeling (DOL) were determined by comparison of native and conjugated antibody masses, using BioPharma Finder 4.1 software.

FPLC purification of the conjugates was performed on an Äkta Pure 25 M chromatography system (GE Healthcare Life Sciences) equipped with a HiTrap® MabSelect™ column (MabSelect resin, Protein A, cross-linked agarose, column I.D. 7 mm, bed dimensions 7 x 25 mm, bed volume 1 mL). After deposition of the product, the conjugate was washed with 10 mL of PBS pH 7.4 (1 mL/min). The conjugate was then eluted with 5 mL of 25 mM acetic acid (1 mL/min) and collected in 500 µL fractions. Purification was monitored at 280 and 700 nm.

UV-Vis absorbance spectra were recorded on a Varian Cary 50 scan equipped with a Hellma Tray Cell or a UV5Nano spectrophotometer (Mettler Toledo).

NIRF imaging was performed using the KIS800 camera from Kaer Labs.

**Reagents**

All chemicals, unless otherwise noted, were acquired from Sigma-Aldrich, Acros Organics and Alfa Aesar and used without further purification. All water used was ultra-pure (>18.2 $M\Omega.cm^{-1}$).

**Synthesis of the MOMIP**

*DFO-NH-Tz-Cl* **3**

Desferrioxamine mesylate salt **1** (1 equiv., 229 µmol, 150 mg) was added to a solution of 3,6-dichloro-1,2,4,5-tetrazine **2** (1.2 equiv., 275 µmol, 41.3 mg) in dry DMSO (3 mL) with N,N-diisopropylethylamine (4 equiv., 915 µmol, 160 µL). The reaction mixture was stirred at room temperature for 1 hour and purified on semi-preparative HPLC on a BetaBasic-18 column (A: $H_2O$ 0.1% TFA, B: MeCN 0.1% TFA; with the following gradient program: 2% of B for 8 min, 2 to 30% in 5 min, 30 % to 60% of B in 60 min, at a flow rate of 20 mL/min) to obtain an orange solid after lyophilization (m = 102 mg, y = 66%).

RP-HPLC-MS: tr = 4 min, m/z calculated for $C_{27}H_{48}ClN_{10}O_8$ $[M+H]^+$ 675.3, found 675.6.

$^1$H NMR (500 MHz, DMSO-$d_6$) δ 9.63 (s, 3H), 8.84 (t, *J* = 5.7 Hz, 1H), 7.77 (m, 2H), 3.50-3.46 (m, 4H), 3.36 (q, *J* = 6.7 Hz, 4H), 2.99 (q, *J* = 6.6 Hz, 4H), 2.57 (t, *J* = 7.4 Hz, 4H), 2.26 (t, *J* = 7.3 Hz, 4H), 1.96 (s, 3H), 1.64-1.56 (m, 2H), 1.56-1.44 (s, 6H), 1.42-1.34 (m, 4H), 1.33-1.28 (m, 2H), 1.26-1.16 (m, 4H). $^{13}$C NMR (126 MHz, DMSO-$d_6$) δ 172.1 (C), 171.4 (C), 170.3 (C), 161.4 (C), 158.5 (C), 47.1 ($CH_2$), 46.9 ($CH_2$), 40.7 ($CH_3$), 38.5 ($CH_2$), 30.0 ($CH_2$), 28.9 ($CH_2$), 27.7 ($CH_2$), 27.6 ($CH_2$), 26.1 ($CH_2$), 23.5 ($CH_2$), 23.5 ($CH_2$), 20.4 ($CH_2$).

*DFO-NH-Tz-S-NH$_2$* **5**

To a solution of DFO-NH-Tz-Cl **3** (1 equiv., 89 µmol, 60 mg) in DMF (2 mL) and DIPEA (8 equiv., 712 µmol, 124 µL) was added a solution of tert-butyl (2-mercaptoethyl)carbamate **4** (1.2 equiv., 107 µmol, 19 mg) in DMF (2.5 mL). The resulting orange solution was stirred at room temperature. After 2 h, the product was precipitated from diethyl ether, redissolved into 2 mL of $CH_2Cl_2$ and 2 mL of TFA and the resulting solution was stirred at room temperature for 1 h. After concentration under vacuum the mixture was purified by semi-preparative HPLC on a BetaBasic-18 column (A: $H_2O$ 0.1% TFA, B: MeCN 0.1% TFA; with the following gradient program: 2% of B for 8 min, 2 to 20% in 5 min, 20 % to 55% of B in 40 min, at a flow rate of 20 mL/min) to afford an orange powder (m = 58 mg, y = 90%).

RP-HPLC-MS: $t_r$ = 3.75 min, *m/z* calculated for $C_{29}H_{54}N_{11}O_8S$ $[M+H]^+$ 716.4, found 716.6.

$^1$H NMR (500 MHz, DMSO-$d_6$) δ 9.67-9.61 (m, 3H), 8.48-8.40 (m, 1H), 7.91 (s, 3H), 7.75-7.66 (m, 2H), 3.43-3.37 (m, 8H), 3.31-3.25 (m, 2H), 3.14-3.04 (m, 2H), 2.96-2.87 (m, 4H), 2.50 (t, *J* = 7.3 Hz, 4H), 2.19 (t, *J* = 7.3 Hz, 4H), 1.89 (s, 3H), 1.58-1.49 (m, 2H), 1.49-1.37 (s, 6H), 1.35-1.26 (m, 4H), 1.25-1.20 (m, 2H), 1.19-1.09 (m, 4H). $^{13}$C-NMR (126 MHz, $D_2O$) $\delta$ = 172.0 (C), 171.4 (C), 170.2 (C), 163.2 (C), 161.0 (C), 47.1 ($CH_2$), 46.8 ($CH_2$), 40.4 ($CH_3$), 38.5 ($CH_2$), 38.3

($CH_2$), 29.9 ($CH_2$), 29.9 ($CH_2$), 28.8 ($CH_2$), 27.9 ($CH_2$), 27.6 ($CH_2$), 27.6 ($CH_2$), 27.4 ($CH_2$), 26.1 ($CH_2$), 23.5 ($CH_2$), 20.4 ($CH_2$) ppm.

*DFO-NH-Tz-S-IR800* **7**

To a solution of IRDye800CW **6** (1 equiv., 6.35 µmol, 6.9 mg) and HATU (1.1 equiv., 7.0 µmol, 2.7 mg) in DMF (250 µL) with DIPEA (1.1 equiv., 7.0 µmol, 1.2 µL) was added DFO-NH-Tz-S-$NH_2$ **5** (1.1 equiv., 7.0 µmol, 5.0 mg) in DMF (250 µL). The green solution was stirred at room temperature for 5 hours. After concentration under vacuum, the mixture was purified by semi-preparative HPLC on an Hypersil Gold column (A: TEAB 50 mM, B: MeCN with the following gradient program: 2% of B for 8 min, 2 to 20% in 5 min, 20 % to 55% of B in 50 min, at a flow rate of 3.5 mL/min) to give a blue/green powder (m = 8.4 mg, y = 78%). RP-HPLC-MS: $t_r$ = 3.6 min., *m/z* calculated for $C_{75}H_{106}N_{13}O_{22}S_5$ $[M+H]^+$ 1700.6, found 1700.9, *m/z* calculated for $[M+2H]^{2+}$ 850.8, found 851.3. HRMS: *m/z* calculated for $C_{75}H_{106}N_{13}O_{22}S_5$ $[M+H]^+$ 1700.61734, found 1700.62481, *m/z* calculated for $[M+2H]^{2+}$ 850.81231, found 850.81535, *m/z* calculated for $[M-H]^-$ 1698.60279, found 1698.60632, *m/z* calculated for $[M-2H]^{2-}$ 848.79776, found 848.80066 .

**Production of recombinant xiRA63 and xiRB49**

The two murine antibodies, Rendomab A63 and Rendomab B49, were chimerized in order to anticipate and minimize the immunogenicity problems for their potential future use in the human clinic. In this context, the variable heavy chain (VH) and variable light chain (VL) regions were fused with the respective constant IgG1 and Kappa regions of the trastuzumab. Plasmids were then co-transfected into ExpiCHO-S cells which were cultured accordingly to the manufacturer's instructions (ThermoFisher-A29127). Twelve days post-transfection, the production of the xiRA63 or xiRB49 were collected and purified using a HiTrap Protein A HP column (GE Healthcare-17-0402-03) following the manufacturer's instructions.

**Synthesis of the immunoconjugates**

*Deglycosylation*

Deglycosylation of xiRA63 or xiRB49 (500 µg, 125 µL) was performed by adding 5 units of recombinant PNGaseF enzyme (New England BioLabs, Ipswich, MA) per 1 µg of mAb (5 µL, 500 U/µL), 25 µL 50 mM sodium phosphate, pH 7.5 (GlycoBuffer 2 10x from New England

Biolabs) and water to make a total volume reaction of 250 μL. The reaction was incubated at 37 °C for 3 h and then purified via size exclusion chromatography (Sephadex G-25 M, PD-10 column, GE Healthcare) and concentrated using centrifugal filter units with a 50,000 Da molecular weight cut off (Amicon™ Ultra 2 mL Centrifugal Filtration Units, Millipore Corp., Billerica, MA) and phosphate buffered saline (PBS, pH 7.4) to obtain the deglycosylated antibodies.

*Enzymatic bioconjugation with MTGase*

To a solution of deglycosylated antibody in PBS was added TCO-$PEG_4$-$NH_2$ **8** (60 equiv. at 60 mM in PBS), MTGase (5 U/mg of antibody, Zedira) and phosphate buffered saline (PBS, pH 7.4) to adjust the antibody concentration to 7.5 g/L. The reaction was incubated at 25 °C for 2 h and then purified via size exclusion chromatography (Sephadex G-25 M, PD-10 column, GE Healthcare) and concentrated using centrifugal filter units with a 50,000 Da molecular weight cut off (Amicon™ Ultra 2 mL Centrifugal Filtration Units, Millipore Corp., Billerica, MA) and phosphate buffered saline (PBS, pH 7.4) to give the TCO-bearing antibodies. Degrees of labeling were estimated by mass spectrometry (Fig S1-2).

*Inverse electron demand Diels-Alder reaction*

To a solution of TCO-bearing antibody in PBS was added the MOMIP DFO-NH-Tz-S-IR800 **7** (20 equiv. *per* accessible TCO at 30 mM in DMSO) and the antibody concentration was adjusted to 5 g/L with phosphate buffered saline (PBS, pH 7.4). The reaction mixture was stirred at room temperature overnight and purified by Protein A affinity chromatography (Hitrap Mabselect Xtra column,Cytiva) to give the immunoconjugates **9** and **10**. Degrees of labeling were measured by UV spectroscopy and mass spectrometry (Fig S1-2).

**Flow cytometry**

We used the protocol of Herbet et al.[30] Briefly, three cell lines were used to assess the apparent affinity of xiRA63 or xiRB49: Chinese hamster ovary wild-type (CHO-WT) cells and CHO cells stably transfected either with human $ET_A$ (CHO-$ET_A$) or human $ET_B$ (CHO-$ET_B$). Apparent affinity was determined with a dilution range from 0.001 nM to 50 nM for xiRA63 and 0.01 nM to 125 nM for xiRB49. The binding was revealed by an Alexa-Fluor 488™ conjugated with F(ab')$_2$-goat anti-human IgG Fc (Invitrogen) and incubated for 4 hours at 4°C. Samples were washed three times with PBS between each step. Sample fluorescence was measured at 488 nm with the FACSCalibur flow cytometer (BD Biosciences) and

expressed as a percentage of the mean fluorescence intensity per sample. The "one site specific binding" function of GraphPad was applied to fit the binding curve and determine the $B_{max}$ and the apparent $K_D$ values. To compared two data group, a statistical Student t test (two-tailed) was carried out (* P < 0.05, ** P < 0.01, *** P < 0.001, **** P < 0.0001).

**Animals**

All animal experiments were performed according to the European Directive 2010/63/EU. The experimental protocol was approved by a local ethics committee for animal use (CETEA) and by the French ministry of agriculture (authorization APAFIS#34522-202201041208791 5v1)/ethics committee n°44). Twelve female 4 weeks old NMRI nude mice (Janvier Labs) were subcutaneously implanted with $5.10^6$ CHO-$ET_A$, CHO-$ET_B$ or CHO-WT cells in the shoulder. Animal anesthesia was performed with 2.5 % of isoflurane in oxygen associated with local xylocaine anesthesia.

When the tumor volume reached about 65 $mm^3$, mice were injected intravenously in the tail vein with either xiRA63-MOMIP or xiRB49-MOMIP (100 µg in a volume of 100 µL in PBS (pH 7.4)).

**NIRF imaging**

At 4 h, 24 h, 48 h, 72 h, and 168 h after injection, animals were imaged using the Kaer Imaging System 800 camera from Kaer Labs (exposure time = 300 ms for xiRA63 and 100 ms for xiRB49). 7 days post-injection, animals were euthanized and fluorescence guided resection of tumors was performed. After the surgery, key organs were collected (liver, spleen, stomach, intestine, heart, kidney, muscle and bones) and imaged to obtain an *ex vivo* biodistribution (exposure time = 800 ms for xiRA63 and 400 ms for xiRB49).

**Statistics**

GraphPad Prism software (v9.0.1) was used for statistical analyzes. Student t test (two-tailed) were carried out to compare two data groups (* P < 0.05, ** P < 0.01, *** P < 0.001, **** P < 0.0001).

**RESULTS AND DISCUSSION**

**Synthesis of the immunoconjugates**

The first step of the synthesis of the immunoconjugates consists in the preparation of a MOnomolecular Multimodal Imaging Probe (MOMIP) containing both a fluorophore and a chelating agent for further $^{89}$Zr radiolabeling. This so-called "multifunctional, single attachment point" (MSAP) design has proven to be the most elegant way to introduce two different functionalities on a biovector, since it allows a perfect control of the ratio between the two functional groups and a better reproducibility of the synthesis when compared to sequential introduction of the two functionalities.[23,28,31,32] We have chosen IRDye800CW as a fluorophore since it is a water-soluble, near-infrared cyanine-based dye (excitation 775 nm, emission 795 nm) that has been extensively studied in clinical trials for Fluorescence Guided Surgery (FGS).[33–36] This dye has been shown to be safe and capable of providing robust tumor-to-background contrast during surgery. To allow further $^{89}$Zr radiolabeling, Desferrioxamine (DFO) was chosen as chelating agent. Although not ideal for $^{89}$Zr chelation, DFO is by far the most commonly used chelator in $^{89}$Zr immunoPET clinical trials[37]. In order to bring together IRDye800CW and DFO in a single molecule, ready to be conjugated, we used a tetrazine platform that was recently developed in our group.[31,32] The MOMIP DFO-NH-Tz-S-IR800 **7** was obtained in three steps (Scheme 1). In the first step, DFO-$NH_2$ **1** was reacted with 3,6-dichloro-1,2,4,5-tetrazine **2** to yield the monosubstituted tetrazine **3** in 66% yield. The first functionalization of the tetrazine ring deactivates the reactivity of the second chlorine atom towards $SN_{Ar}$ reaction. Thus, a stronger nucleophile, the thiol **4**, was used to prepare the difunctionalized tetrazine **5** in 90% yield. In the last step, **5** was reacted with the commercially available IRDye800-COOH **6** to give the aimed compound **7** in 78% yield.

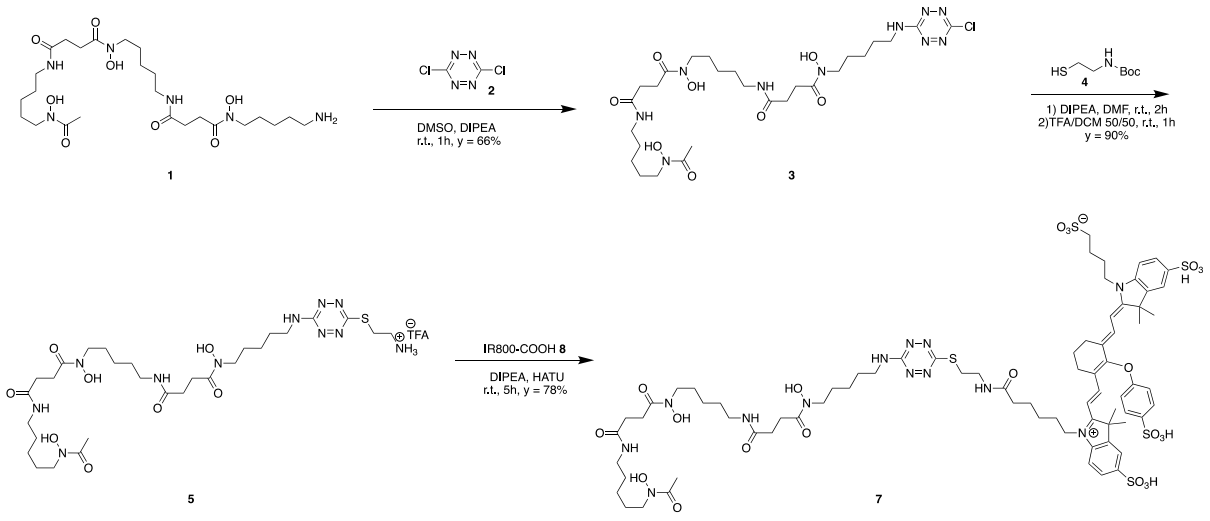


*Scheme 1: Synthesis of the MOMIP DFO-NH-Tz-S-IR800*

The conjugation of DFO-NH-Tz-S-IR800 **7** to xiRA63 and xiRB49 requires the prior introduction on the antibodies of a click partner for iEDDA reaction. *Trans*-cyclooctene (TCO) / tetrazine ligation has been extensively studied[38–41] and we decided to functionalize the antibodies with TCO moieties in a site-specific way. Indeed, the superiority of site-specific conjugation vs. random conjugation on lysine residues has been well established, leading to much more chemically defined and homogeneous conjugates.[28,29] Among the existing site-specific conjugation methods, we have chosen the efficient enzymatic ligation of amine derivatives on the heavy chain of IgGs catalyzed by transglutaminase (MTGase) (Scheme 2).[42,43] Besides being affordable, this technique requires to remove the glycan chains located in positions N297, which could help reducing off-target uptake in the liver and spleen thanks to an impaired FcγRI binding.[44,45] This feature might be interesting as fluorophores have a tendency to increase the liver uptake due to their hydrophobicity. After quantitative deglycosylation of xiRA63 and xiRB49 using PNGaseF enzyme (Fig S2), the coupling of TCO-$PEG_4$-$NH_2$ **8** to the antibodies in positions Q295 was performed using transglutaminase. Finally, the iEDDA reaction of DFO-NH-Tz-S-IR800 **7** with the TCO-modified antibodies was performed prior to the injection to yield the aimed bimodal antibody conjugates xiRA63-MOMIP **9** and xiRB49-MOMIP **10**.

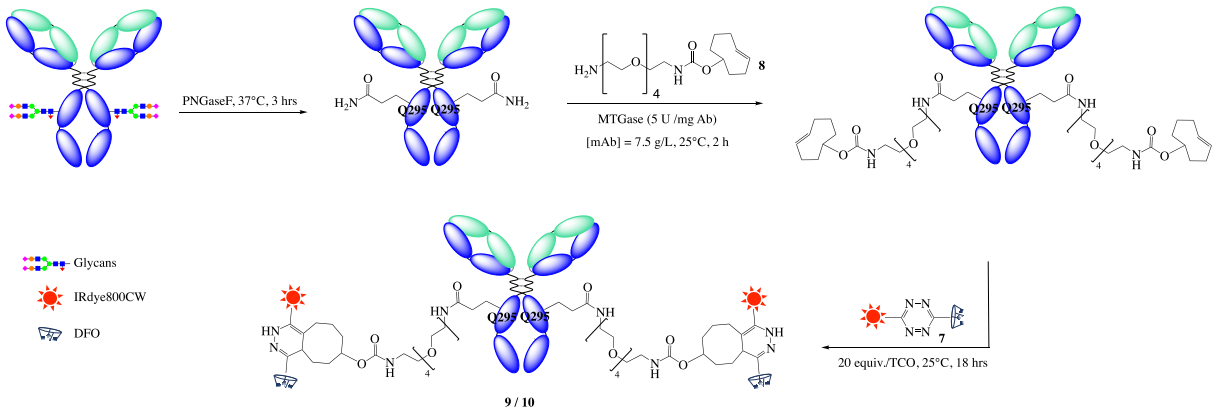


*Scheme 2: Synthesis of the immunoconjugates xiRA63-MOMIP **9** and xiRB49-MOMIP **10***

The number of MOMIP per antibody, called Degree of Labeling (DOL), was determined by UV-spectroscopy, using the integral method described by Grabolle *et al.*,[46] and by mass

spectrometry. Briefly, the immunoconjugates were digested with the IDES enzyme and a detailed mass spectrometry characterization was performed by liquid chromatography–mass spectrometry middle-down analyses of Fc/2 fragments (Fig S3-4). The values obtained for xiRA63-MOMIP **9** and xiRB49-MOMIP **10** were 1.6 ≤ DOL ≤ 1.9 and 1.6 ≤ DOL ≤ 1.7, respectively, which are closed to the theoretically expected value of 2 (Table 1). Besides, as shown on the UV chromatogram at 780nm, we confirmed that the conjugation only took place on the Fc fragment.

*Table 1: Degree of labeling of xiRA63-MOMIP **9** and xiRB49-MOMIP **10** determined by UV-spectroscopy and mass spectrometry.*

| ***Degree of labeling*** | ***UV*** | ***Mass spectrometry*** |
|---|---|---|
| *xiRA63-MOMIP **9*** | *1.9 ±0.1* | *0.8 ×2 = 1.6* |
| *xiRB49-MOMIP **10*** | *1.7 ±0.1* | *0.8 ×2 = 1.6* |

***In vitro* studies**

The next step was to assess the binding affinity of xiRA63-MOMIP **9** and xiRB49-MOMIP **10** to CHO-$ET_A$ and CHO-$ET_B$ cells, respectively. This was performed by flow cytometry. The binding curves as well as the binding affinity constants ($K_{DAPP}$ and Bmax) are reported on an indicative basis in Fig. 1. No loss of binding potential was observed between the MOMIP conjugates and the native antibodies (subnanomolar range), confirming that site-specific conjugation of the MOMIP to the antibodies did not affect the functionality of both xiRA63 and xiRB49 for their target.

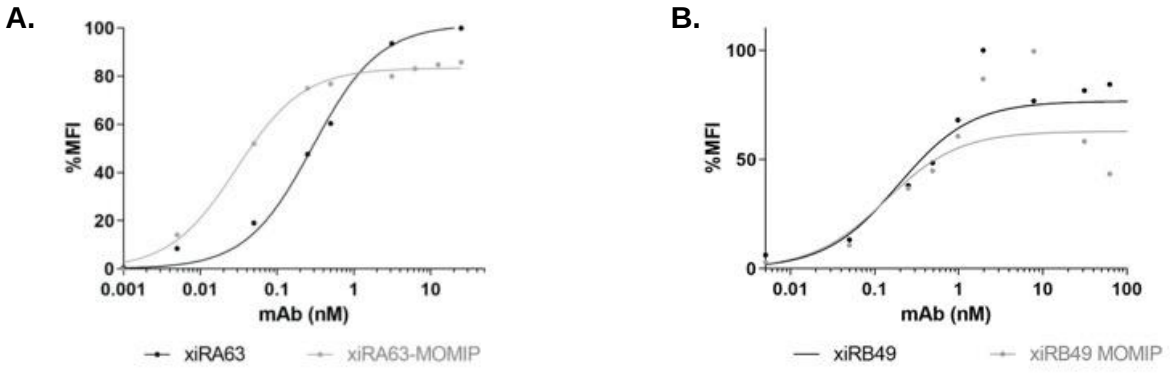


**C.**

| | xiRA63 | xiRA63-MOMIP 9 | xiRB49 | xiRB49-MOMIP 10 |
|---|---|---|---|---|
| Bmax (%MFI) | 101.5 | 83,4 | 76.7 | 62.9 |
| $K_{Dapp}$ (nM) | 0.290 | 0.030 | 0.191 | 0.136 |

*Figure 1: Characterization of the MOMIP conjugation impact onto the xiRA63 and the xiRB49.* ***A****. Binding curve comparison of the xiRA63 (black curve) and the xiRA63-MOMIP* ***9*** *(grey curve) by flow cytometry.* ***B****. Binding curve comparison of the xiRB49 (black curve) and the xiRB49-MOMIP* ***10*** *(grey curve) by flow cytometry.* ***C****. Apparent binding affinities and Bmax of xiRA63, xiRB49 and the corresponding MOMIP conjugates* ***9*** *and* ***10****. ~~Data are presented as mean ± SEM. A two-tailed paired Student t test was used for data comparison.~~ MFI: Median Fluorescence Intensity, mAb: concentration of the monoclonal antibody.*

### *In vivo* and *ex vivo* evaluation

CHO-$ET_A$ and CHO-$ET_B$ cells were subcutaneously implanted in the right shoulder of nude mice. A third group of animals was implanted with CHO cells which present no expression of ET human receptors (CHO-WT). After 5 to 7 days after implantation, xiRA63-MOMIP **9** was injected intravenously in a group of mice bearing $ET_A^+$ tumors (n=3), xiRB49-MOMIP **10** was injected in a group of mice bearing $ET_B^+$ tumors (n=3), and both conjugates were injected in mice bearing CHO-WT tumors (2 groups of 3 mice) as a negative control (NC). Fluorescence images were recorded at 4h, 24h, 48h, 72h and 7 days post injection (Figure 2).

The images show a clear fluorescent signal in the CHO-$ET_A$ and CHO-$ET_B$ tumors 24h post-injection, while the signal is barely distinguishable in CHO-WT tumors, demonstrating that the high affinity and specificity of the conjugates for their target is maintained *in vivo*. It has to be noted that the background is a bit brighter in the images of mice injected with xiRA63-MOMIP **9** because of a longer exposure time (300 ms vs. 100 ms for the mice injected with xiRB49-MOMIP **10**).

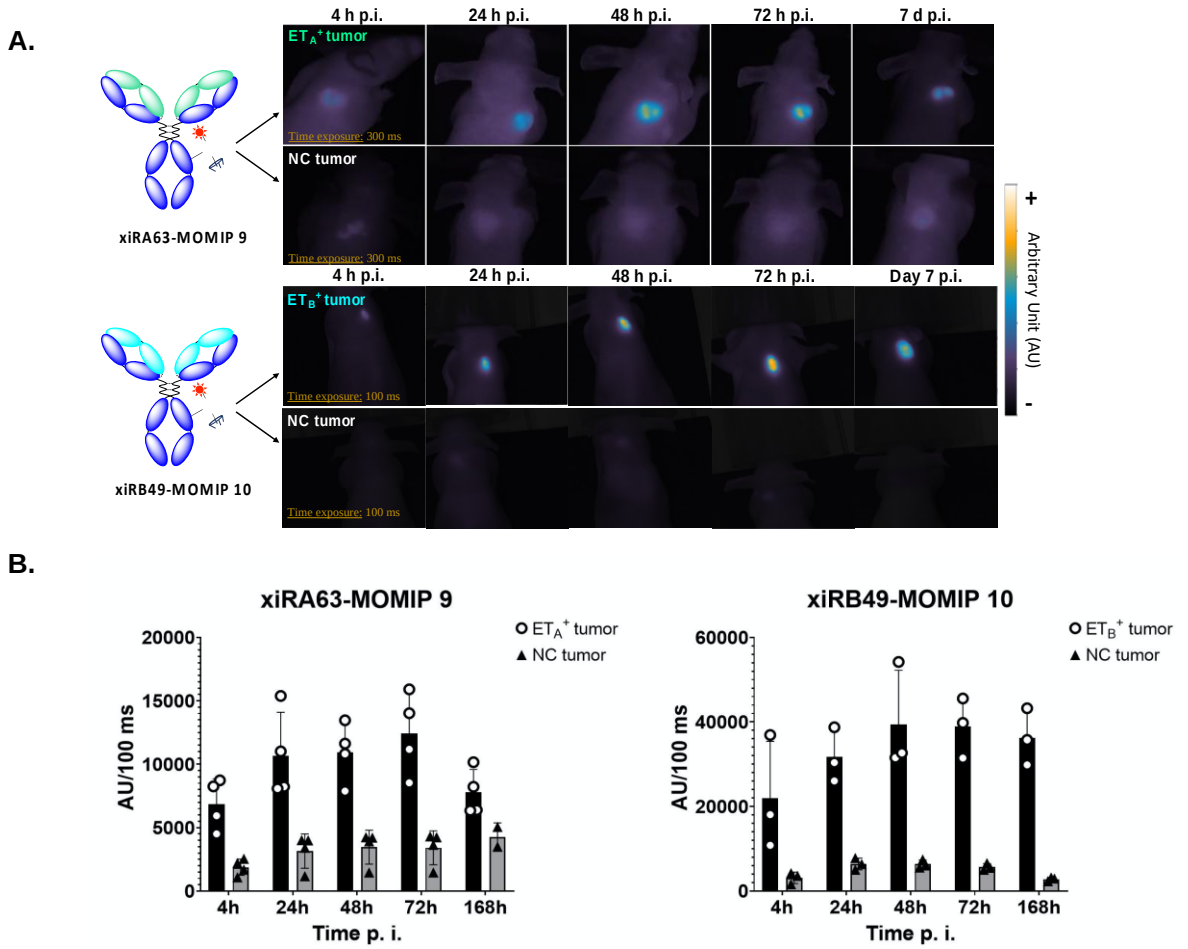


*Figure 2:* ***NIRF experiments. A.*** *Longitudinal study of the emitted fluorescence after i.v. injection of xiRA63-MOMIP 9 (top) and xiRB49-MOMIP 10 (bottom) conjugates in $ET_A^+$, $ET_B^+$ and NC tumors bearing mice.* ***B.*** *Tumor mean fluorescence intensity over the 7 days.*

A relative quantification of the fluorescence intensity was estimated at different time points (Figure 3, Table S1). These data illustrate the specific uptake of xiRA63-MOMIP **9** and xiRB49-MOMIP **10** in mice bearing CHO-$ET_A$ and CHO-$ET_B$ tumors, respectively, and prove that the accumulation of the conjugates in the tumors is not due to passive targeting as no signal was observed in NC tumors. It can also be seen that maximum fluorescence intensity is obtained around 48h post-injection of the conjugates and maintained up to 7 days post-injection.

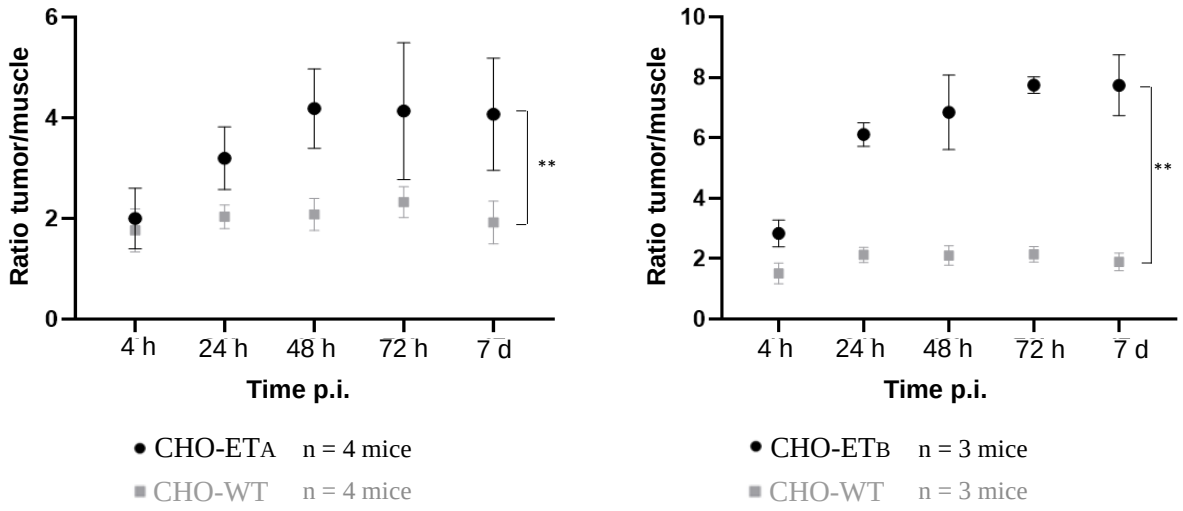


*Figure 3: Tumor/background ratio of the fluorescence intensity for xiRA63-MOMIP **9** (left) and xiRB49-MOMIP **10** (right)*

After the last *in vivo* imaging 7 days post-injection, mice were sacrificed and tumors resection was successfully performed under the Kaer Imaging System 800, an open fluorescence imaging system adapted to intraoperative imaging on small animals (Fig. 4, Video S1-2). Thanks to the fluorescence signal, tumor margins were clearly delineated and we were able to spot and remove residual $ET_B^+$ cells that would have been missed with white light.

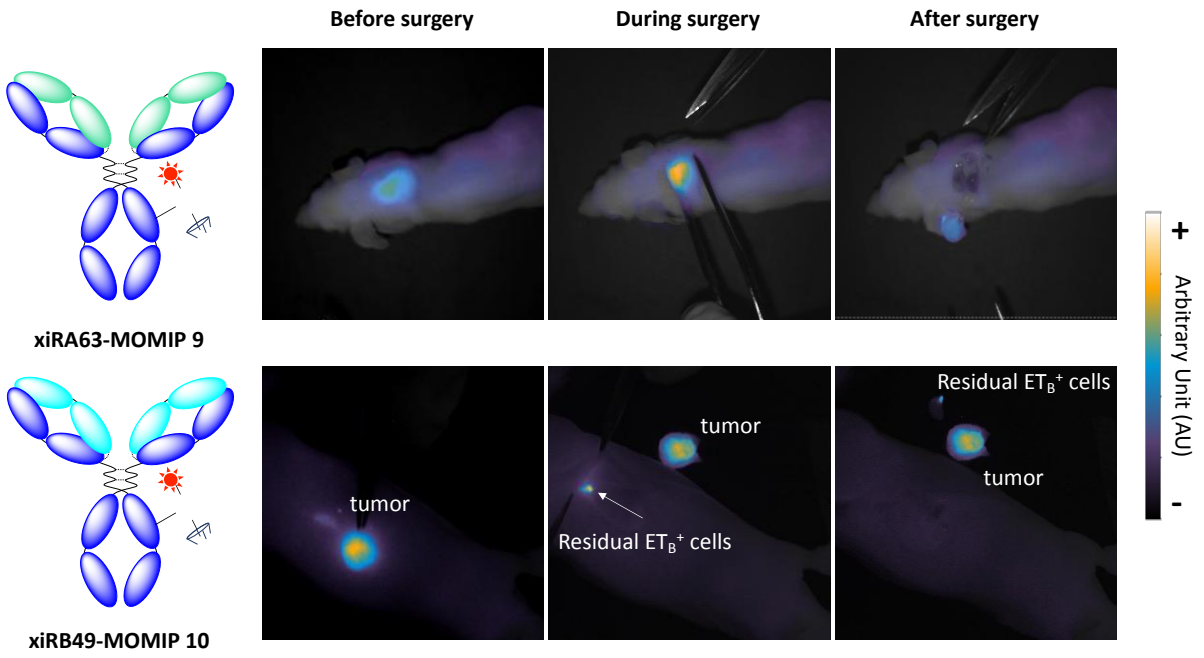


*Figure 4: Fluorescence guided surgery of $ET_A^+$ (top) and $ET_B^+$ (bottom) tumors in nude mice. Images were recorded with a Kaer Imaging system 800 (excitation 785 nm – emission: high pass filter > 810).*

Major organs were also collected and fluorescence images were recorded (Fig. 5, Table S2). It is clear from these images that while the tumors overexpressing ET receptors are very bright, no or very weak fluorescence is observed in organs or NC tumors. In particular, no significant signal can be observed in the liver, which can be the case when using organic fluorescent dyes. These data are consistent with PET imaging data obtained with a $^{89}$Zr-DFO-xiRA63 conjugate, showing that the enzymatic conjugation of the fluorescent dye did not affect the biodistribution of the antibody.[10]

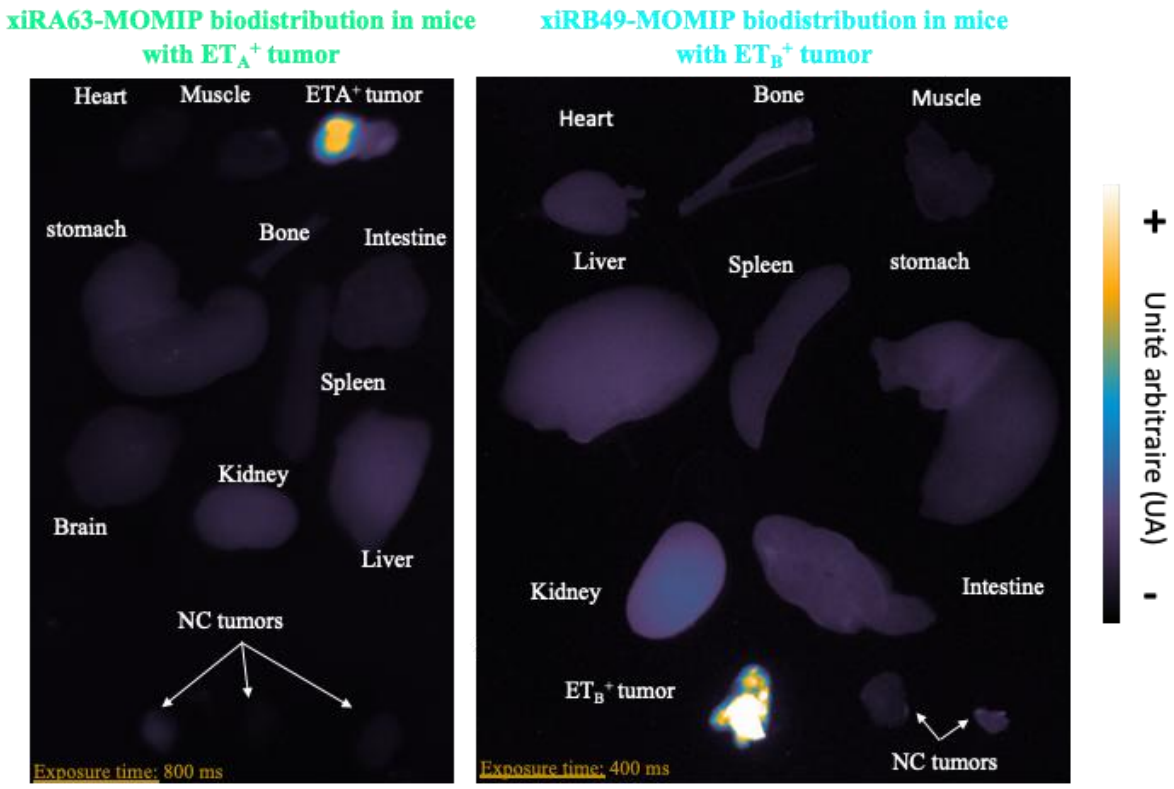


*Figure 5: Fluorescence imaging of the different organs and tumors. $ET_A^+$ tumor bearing mouse injected with xiRA63-MOMIP **9** (left) and $ET_B^+$ tumor bearing mouse injected with xiRB49-MOMIP **10** (right). In both cases, a NCT tumor was added.*

## CONCLUSION

Two bimodal immunoconjugates targeting endothelin receptors $ET_A$ and $ET_B$ were prepared. Site-specific conjugation of a multifunctional monomolecular imaging probe (MOMIP) allowed the synthesis of chemically defined and homogenous conjugates. IRDye800CW and DFO were brought together into a tetrazine platform that is highly versatile and could enable the use of any other dye/chelator combination. The careful control of the modification of the antibodies resulted in immunoconjugates that retain their affinity and specificity for their target, as shown by *in vitro* and *in vivo* experiments. In particular, fluorescence images of mice with subcutaneously implanted $ET_A^+$ and $ET_B^+$ tumors showed a strong and selective accumulation of the immunoconjugates in the tumors. These preliminary results are very promising and we now wish to investigate these new bimodal conjugates in an orthotopic mouse model of glioblastoma to demonstrate their potential as i) a tool for the diagnosis and stratification of patients thanks to PET imaging and ii) a support to help visualizing tumor margins during surgery thanks to the fluorescence.

## FUNDING

This study received funding from the French Research National Agency (ANR) via the project PRCE “DualmAb” (ANR-19-CE18-0013). Support was also provided by the Conseil Régional de Bourgogne Franche-Comté (program “Multimod”, 2020Y-08126, 2019Y-10589) and the European Union through the PO FEDER-FSE Bourgogne 2014/2020 (n° BG0026681).

## ACKNOWLEDGMENTS

The authors thank the “Plateforme d’Analyse Chimique et de Synthèse Moléculaire de l’Université de Bourgogne” (PACSMUB, http://www.wpcm.fr) for access to analytical instrumentation, Marie-José Penouilh (University of Burgundy, PACSMUB) and Dr. Quentin Bonnin (University of Burgundy, PACSMUB) for the small molecules high-resolution mass spectrometry, and Dr. Michael Claron for the antibody high-resolution mass spectrometry.

## REFERENCES

(1) Yanagisawa, M.; Kurihara, H.; Kimura, S.; Tomobe, Y.; Kobayashi, M.; Mitsui, Y.; Yazaki, Y.; Goto, K.; Masaki, T. A Novel Potent Vasoconstrictor Peptide Produced by Vascular Endothelial Cells. *Nature* **1988**, *332* (6163), 411–415.

(2) Nelson, J.; Bagnato, A.; Battistini, B.; Nisen, P. The Endothelin Axis: Emerging Role in Cancer. *Nat. Rev. Cancer* **2003**, *3* (2), 110–116.

(3) Bagnato, A.; Spinella, F.; Rosanò, L. The Endothelin Axis in Cancer: The Promise and the Challenges of Molecularly Targeted Therapy. *Can. J. Physiol. Pharmacol.* **2008**, *86* (8), 473–484.

(4) Rosanò, L.; Spinella, F.; Bagnato, A. The Importance of Endothelin Axis in Initiation, Progression, and Therapy of Ovarian Cancer. *Am. J. Physiol.-Regul. Integr. Comp. Physiol.* **2010**, *299* (2), 395–404.

(5) Irani, S.; Salajegheh, A.; Smith, R. A.; Lam, A. K.-Y. A Review of the Profile of Endothelin Axis in Cancer and Its Management. *Crit. Rev. Oncol. Hematol.* **2014**, *89* (2), 314–321.

(6) Hanahan, D. Hallmarks of Cancer: New Dimensions. *Cancer Discov.* **2022**, *12* (1), 31–46.

(7) Bagnato, A.; Loizidou, M.; Pflug, B.; Curwen, J.; Growcott, J. Role of the Endothelin Axis and Its Antagonists in the Treatment of Cancer. *Br. J. Pharmacol.* **2011**, *163* (2), 220–233.

(8) Boquet, D.; Ducancel, F.; Herbet, A.; Costa, N.; Hugnot, J.-P. Antibodies against Endothelin Receptor B Subtype B and Uses Thereof. FR3053042A1, December 29, 2017. https://patents.google.com/patent/FR3053042A1/en (accessed 2023-05-02).

(9) Boquet, D.; Herbet, A.; Ducancel, F.; Costa, N.; Couraud, J.-Y.; Hugnot, J.-P. Antibody against the Endothelin Receptor Subtype A, and Uses Thereof. WO2019155151A2, August 15, 2019. https://patents.google.com/patent/WO2019155151A2/en (accessed 2023-05-02).

(10) Hautiere, M.; Vivier, D.; Pineau, D.; Denis, C.; Kereselidze, D.; Herbet, A.; Costa, N.; Goncalves, V.; Selingue, E.; Larrat, B.; Hugnot, J. P.; Denat, F.; Boquet, D.; Truillet, C. ImmunoPET Imaging–Based Pharmacokinetic Profiles of an Antibody and Its Fab Targeting Endothelin A Receptors on Glioblastoma Stem Cells in a Preclinical Orthotopic Model. *Eur. J. Nucl. Med. Mol. Imaging* **2023**. 10.1007/s00259-023-06268-3
(11) Miller, K. D.; Nogueira, L.; Devasia, T.; Mariotto, A. B.; Yabroff, K. R.; Jemal, A.; Kramer, J.; Siegel, R. L. Cancer Treatment and Survivorship Statistics, 2022. *CA. Cancer J. Clin.* **2022**, *72* (5), 409–436.
(12) Nagaya, T.; Nakamura, Y. A.; Choyke, P. L.; Kobayashi, H. Fluorescence-Guided Surgery. *Front. Oncol.* **2017**, *7:314*.
(13) Stewart, H. L.; Birch, D. J. S. Fluorescence Guided Surgery. *Methods Appl. Fluoresc.* **2021**, *9* (4).
(14) Napier, T. S.; Udayakumar, N.; Jani, A. H.; Hartman, Y. E.; Houson, H. A.; Moore, L.; Amm, H. M.; van den Berg, N. S.; Sorace, A. G.; Warram, J. M. Comparison of Panitumumab-IRDye800CW and 5-Aminolevulinic Acid to Provide Optical Contrast in a Model of Glioblastoma Multiforme. *Mol. Cancer Ther.* **2020**, *19* (9), 1922–1929.
(15) Rosenthal, E. L.; Warram, J. M.; de Boer, E.; Chung, T. K.; Korb, M. L.; Brandwein-Gensler, M.; Strong, T. V.; Schmalbach, C. E.; Morlandt, A. B.; Agarwal, G.; Hartman, Y. E.; Carroll, W. R.; Richman, J. S.; Clemons, L. K.; Nabell, L. M.; Zinn, K. R. Safety and Tumor-Specificity of Cetuximab-IRDye800 for Surgical Navigation in Head and Neck Cancer. *Clin. Cancer Res.* **2015**, *21* (16), 3658–3666.
(16) Nagengast,W.B. *Visualization of a VEGF-Targeted Near-Infrared Fluorescent Tracer in Patients With Familial Adenomatous Polyposis During Fluorescence Endoscopy A Single Center Pilot Intervention Study*; Clinical trial registration NCT02113202; clinicaltrials.gov, 2016. https://clinicaltrials.gov/ct2/show/NCT02113202 (accessed 2023-04-30).
(17) Gao, R. W.; Teraphongphom, N.; de Boer, E.; van den Berg, N. S.; Divi, V.; Kaplan, M. J.; Oberhelman, N. J.; Hong, S. S.; Capes, E.; Colevas, A. D.; Warram, J. M.; Rosenthal, E. L. Safety of Panitumumab-IRDye800CW and Cetuximab-IRDye800CW for Fluorescence-Guided Surgical Navigation in Head and Neck Cancers. *Theranostics* **2018**, *8* (9), 2488–2495.
(18) Technical University of Munich. *Improvement of the Operative Outcome in Patients With Primary VEGF Positive Unifocal Breast Cancer or Ductal Carcinoma in Situ (DCIS) Through the Intraoperative Visualization of the Tumor Using Molecular Imaging and Fluorescent Markers Bevacizumab-IRDye-800CW*; NCT05359874; 2022. https://clinicaltrials.gov/ct2/show/NCT05359874 (accessed 2023-04-30).
(19) Seibold, U.; Wängler, B.; Schirrmacher, R.; Wängler, C. Bimodal Imaging Probes for Combined PET and OI: Recent Developments and Future Directions for Hybrid Agent Development. *BioMed Res. Int.* **2014**, *2014*, 153741.
(20) van Leeuwen, F. W. B.; Schottelius, M.; Brouwer, O. R.; Vidal-Sicart, S.; Achilefu, S.; Klode, J.; Wester, H.-J.; Buckle, T. Trending: Radioactive and Fluorescent Bimodal/Hybrid Tracers as Multiplexing Solutions for Surgical Guidance. *J. Nucl. Med.* **2020**, *61* (1), 13–19.
(21) Li, D.; Zhang, J.; Chi, C.; Xiao, X.; Wang, J.; Lang, L.; Ali, I.; Niu, G.; Zhang, L.; Tian, J.; Ji, N.; Zhu, Z.; Chen, X. First-in-Human Study of PET and Optical Dual-Modality Image-Guided Surgery in Glioblastoma Using $^{68}$Ga-IRDye800CW-BBN. *Theranostics* **2018**, *8* (9), 2508–2520.
(22) Renard, E.; Dancer, P.-A.; Portal, C.; Denat, F.; Prignon, A.; Goncalves, V. Design of Bimodal Ligands of Neurotensin Receptor 1 for Positron Emission Tomography Imaging and Fluorescence-Guided Surgery of Pancreatic Cancer. *J. Med. Chem.* **2020**, *63* (5), 2426–2433.
(23) Privat, M.; Bellaye, P.-S.; Lescure, R.; Massot, A.; Baffroy, O.; Moreau, M.; Racoeur, C.; Marcion, G.; Denat, F.; Bettaieb, A.; Collin, B.; Bodio, E.; Paul, C.; Goze, C.

Development of an Easily Bioconjugatable Water-Soluble Single-Photon Emission-Computed Tomography/Optical Imaging Bimodal Imaging Probe Based on the Aza-BODIPY Fluorophore. *J. Med. Chem.* **2021**, *64* (15), 11063–11073.
(24) Azhdarinia, A.; Ghosh, P.; Ghosh, S.; Wilganowski, N.; Sevick-Muraca, E. M. Dual-Labeling Strategies for Nuclear and Fluorescence Molecular Imaging: A Review and Analysis. *Mol. Imaging Biol.* **2012**, *14* (3), 261–276.
(25) Ariztia, J.; Solmont, K.; Moïse, N. P.; Specklin, S.; Heck, M. P.; Lamandé-Langle, S.; Kuhnast, B. PET/Fluorescence Imaging: An Overview of the Chemical Strategies to Build Dual Imaging Tools. *Bioconjug. Chem.* **2022**, *33* (1), 24–52.
(26) Rijpkema, M.; Bos, D. L.; Cornelissen, A. S.; Franssen, G. M.; Goldenberg, D. M.; Oyen, W. J.; Boerman, O. C. Optimization of Dual-Labeled Antibodies for Targeted Intraoperative Imaging of Tumors. *Mol. Imaging* **2015**, *14* (7), 348–355.
(27) Kristensen, L. K.; Christensen, C.; Jensen, M. M.; Agnew, B. J.; Schjöth-Frydendahl, C.; Kjaer, A.; Nielsen, C. H. Site-Specifically Labeled 89Zr-DFO-Trastuzumab Improves Immuno-Reactivity and Tumor Uptake for Immuno-PET in a Subcutaneous HER2-Positive Xenograft Mouse Model. *Theranostics* **2019**, *9* (15), 4409–4420.
(28) Adumeau, P.; Raavé, R.; Boswinkel, M.; Heskamp, S.; Wessels, H. J. C. T.; van Gool, A. J.; Moreau, M.; Bernhard, C.; Da Costa, L.; Goncalves, V.; Denat, F. Site-Specific, Platform-Based Conjugation Strategy for the Synthesis of Dual-Labeled Immunoconjugates for Bimodal PET/NIRF Imaging of HER2-Positive Tumors. *Bioconjug. Chem.* **2022**, *33* (3), 530–540.
(29) Privat, M.; Bellaye, P.-S.; Chazeau, E.; Racoeur, C.; Adumeau, P.; Vivier, D.; Bernhard, C.; Moreau, M.; Collin, B.; Bettaieb, A.; Denat, F.; Bodio, E.; Paul, C.; Goze, C. First Comparison Study of the In Vitro and In Vivo Properties of a Randomly and Site-Specifically Conjugated SPECT/NIRF Monomolecular Multimodal Imaging Probe (MOMIP) Based on an Aza-BODIPY Fluorophore. *Bioconjug. Chem.* **2023**, *34* (4), 621–628.
(30) Herbet, A.; Costa, N.; Leventoux, N.; Mabondzo, A.; Couraud, J.-Y.; Borrull, A.; Hugnot, J.-P.; Boquet, D. Antibodies Targeting Human Endothelin-1 Receptors Reveal Different Conformational States in Cancer Cells. *Physiol. Res.* **2018**, *67* (Suppl 1), S257–S264.
(31) Canovas, C.; Moreau, M.; Vrigneaud, J.-M.; Bellaye, P.-S.; Collin, B.; Denat, F.; Goncalves, V. Modular Assembly of Multimodal Imaging Agents through an Inverse Electron Demand Diels–Alder Reaction. *Bioconjug. Chem.* **2019**, *30* (3), 888–897.
(32) Renard, E.; Collado Camps, E.; Canovas, C.; Kip, A.; Gotthardt, M.; Rijpkema, M.; Denat, F.; Goncalves, V.; van Lith, S. A. M. Site-Specific Dual-Labeling of a VHH with a Chelator and a Photosensitizer for Nuclear Imaging and Targeted Photodynamic Therapy of EGFR-Positive Tumors. *Cancers* **2021**, *13* (3), 428.
(33) Rosenthal, E. *Intraoperative Pancreatic Cancer Detection Using Multimodality Molecular Imaging*; Clinical trial registration NCT02736578; clinicaltrials.gov, 2019. https://clinicaltrials.gov/ct2/show/NCT02736578 (accessed 2023-04-30).
(34) Rosenthal, E. *Open-Label Study Evaluating Cetuximab-IRDye800 as an Optical Imaging Agent to Detect Neoplasms During Neurosurgical Procedures*; Clinical trial registration NCT02855086; clinicaltrials.gov, 2020. https://clinicaltrials.gov/ct2/show/NCT02855086 (accessed 2023-04-30).
(35) Witjes, M. J. H. *Image Guided Surgery for Margin Assessment of Head and Neck Cancer Using Cetuximab-IRDye800CW Conjugate*; Clinical trial registration NCT03134846; clinicaltrials.gov, 2021. https://clinicaltrials.gov/ct2/show/NCT03134846 (accessed 2023-04-30).
(36) Bharadwaj, S. *Evaluation of IRDye800CW-Nimotuzumab in Lung Cancer Surgery*; Clinical trial registration NCT04459065; clinicaltrials.gov, 2022.

https://clinicaltrials.gov/ct2/show/NCT04459065 (accessed 2023-04-30).
(37) Heskamp, S.; Raavé, R.; Boerman, O.; Rijpkema, M.; Goncalves, V.; Denat, F. 89Zr-Immuno-Positron Emission Tomography in Oncology: State-of-the-Art 89Zr Radiochemistry. *Bioconjug. Chem.* **2017**, *28* (9), 2211–2223.
(38) Blackman, M. L.; Royzen, M.; Fox, J. M. Tetrazine Ligation: Fast Bioconjugation Based on Inverse-Electron-Demand Diels−Alder Reactivity. *J. Am. Chem. Soc.* **2008**, *130* (41), 13518–13519.
(39) Johann, K.; Svatunek, D.; Seidl, C.; Rizzelli, S.; Bauer, T. A.; Braun, L.; Koynov, K.; Mikula, H.; Barz, M. Tetrazine- and Trans-Cyclooctene-Functionalised Polypept(o)Ides for Fast Bioorthogonal Tetrazine Ligation. *Polym. Chem.* **2020**, *11* (27), 4396–4407.
(40) Ravasco, J. M. J. M.; Coelho, J. A. S.; Trindade, A. F.; Afonso, C. A. M. Synthesis and Reactivity/Stability Study of Double-Functionalizable Strained Trans-Cyclooctenes for Tetrazine Bioorthogonal Reactions. *Pure Appl. Chem.* **2020**, *92* (1), 15–23.
(41) Wang, M.; Wang, H.; Niu, C. Q.; Zhang, T.; Wu, Z.; Li, Z. Tetrazine-TCO Ligation: A Potential Simple Approach to Improve Tumor Uptake through Enhanced Blood Circulation. *Bioconjug. Chem.* **2020**, *31* (7), 1795–1803.
(42) Dennler, P.; Schibli, R.; Fischer, E. Enzymatic Antibody Modification by Bacterial Transglutaminase. *Methods Mol. Biol.* **2013**, *1045*, 205–215.
(43) Dennler, P.; Chiotellis, A.; Fischer, E.; Brégeon, D.; Belmant, C.; Gauthier, L.; Lhospice, F.; Romagne, F.; Schibli, R. Transglutaminase-Based Chemo-Enzymatic Conjugation Approach Yields Homogeneous Antibody-Drug Conjugates. *Bioconjug. Chem.* **2014**, *25* (3), 569–578.
(44) Vivier, D.; Sharma, S. K.; Adumeau, P.; Rodriguez, C.; Fung, K.; Zeglis, B. M. The Impact of FcγRI Binding on Immuno-PET. *J. Nucl. Med.* **2019**, *60* (8), 1174–1182.
(45) Vivier, D.; Fung, K.; Rodriguez, C.; Adumeau, P.; Ulaner, G. A.; Lewis, J. S.; Sharma, S. K.; Zeglis, B. M. The Influence of Glycans-Specific Bioconjugation on the FcγRI Binding and In Vivo Performance of 89Zr-DFO-Pertuzumab. *Theranostics* **2020**, *10* (4), 1746–1757.
(46) Grabolle, M.; Brehm, R.; Pauli, J.; Dees, F. M.; Hilger, I.; Resch-Genger, U. Determination of the Labeling Density of Fluorophore–Biomolecule Conjugates with Absorption Spectroscopy. *Bioconjug. Chem.* **2012**, *23* (2), 287–292.